Article

Current Biology

Structures and roles of BcsD and partner scaffold proteins in proteobacterial cellulose secretion

Graphical abstract

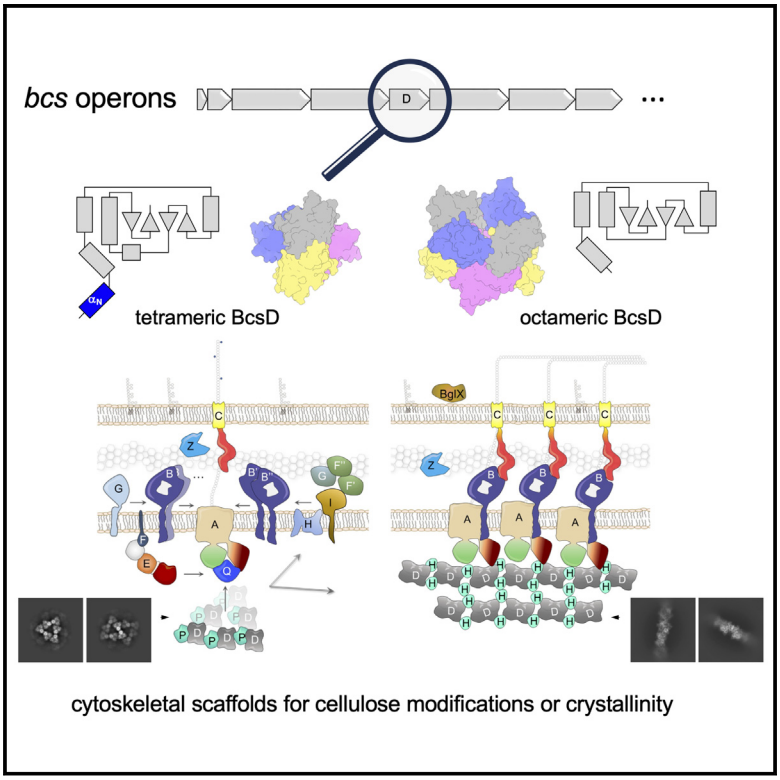

Highlights

- Multiple BcsD cryo-EM structures reveal distinct quaternary structure assemblies
- BcsD- and proline-rich partners assemble BcsD fold-specific cytoskeletal scaffolds
- BcsD-partner scaffolds interact directly with the cellulose synthase complexes
- Resultant synthase arrays may determine polymer properties and biofilm architecture

Authors

Thibault G. Sana, Areti Notopoulou, Lucie Puygrenier, Marion Decossas, Sandra Moreau, Aurélien Carlier, Petya V. Krasteva

Correspondence

pv.krasteva@iecb.u-bordeaux.fr

In brief

Bacterial cellulose is a widespread biofilm matrix constituent secreted by multicomponent Bcs secretion systems. Sana et al. examine the distribution, structure, interactions, and function of the BcsD subunit as an intracellular scaffold builder across Proteobacteria.

Sana et al., 2024, Current Biology *34*, 106–116
January 8, 2024
https://doi.org/10.1016/j.cub.2023.11.057

CellPress

CellPress
OPEN ACCESS

Current Biology

Article

Structures and roles of BcsD and partner scaffold proteins in proteobacterial cellulose secretion

Thibault G. Sana,[1,2,5] Areti Notopoulou,[1,2,5] Lucie Puygrenier,[1,2] Marion Decossas,[1,2] Sandra Moreau,[3] Aurélien Carlier,[3,4] and Petya V. Krasteva[1,2,6,7,*]

[1]Université de Bordeaux, CNRS, Bordeaux INP, CBMN, UMR 5248, Pessac 33600, France
[2]"Structural Biology of Biofilms" Group, European Institute of Chemistry and Biology (IECB), 2 Rue Robert Escarpit, Pessac 33600, France
[3]LIPME, Université de Toulouse, INRAE, CNRS, Castanet-Tolosan 31326, France
[4]Laboratory of Microbiology, Ghent University, Ghent 9000, Belgium
[5]These authors contributed equally
[6]X (formerly Twitter): @krastevalab
[7]Lead contact
*Correspondence: pv.krasteva@iecb.u-bordeaux.fr
https://doi.org/10.1016/j.cub.2023.11.057

SUMMARY

Cellulose is the world's most abundant biopolymer, and similar to its role as a cell wall component in plants, it is a prevalent constituent of the extracellular matrix in bacterial biofilms. Although bacterial cellulose (BC) was first described in the 19th century, it was only recently revealed that it is produced by several distinct types of Bcs secretion systems that feature multiple accessory subunits in addition to a catalytic BcsAB synthase tandem. We recently showed that crystalline cellulose secretion in the *Gluconacetobacter* genus (α-Proteobacteria) is driven by a supramolecular BcsH-BcsD scaffold—the "cortical belt"—which stabilizes the synthase nanoarrays through an unexpected inside-out mechanism for secretion system assembly. Interestingly, while *bcsH* is specific for *Gluconacetobacter*, *bcsD* homologs are widespread in Proteobacteria. Here, we examine BcsD homologs and their gene neighborhoods from several plant-colonizing β- and γ-Proteobacteria proposed to secrete a variety of non-crystalline and/or chemically modified cellulosic polymers. We provide structural and mechanistic evidence that through different quaternary structure assemblies BcsD acts with proline-rich BcsH, BcsP, or BcsO partners across the proteobacterial clade to form synthase-interacting intracellular scaffolds that, in turn, determine the biofilm strength and architecture in species with strikingly different physiology and secreted biopolymers.

INTRODUCTION

Although generally defined as unicellular microorganisms, bacteria constantly exchange substances and information with their confrères and the environment and can efficiently shelter themselves and achieve homeostasis by building collaborative multicellular communities called biofilms. Within a biofilm, bacteria are embedded in complex extracellular matrix composed of proteinaceous fimbriae, extracellular DNA, and exopolysaccharides that provides not only mechanical protection but also an environment for nutrient enrichment, intercellular exchange, and functional differentiation.[1,2] Cellulose—an unbranched homopolymer of β-1,4-linked glucose moieties with exceptionally low chemical complexity but remarkable tensile strength, hydrophilicity, pH tolerance, and porosity—is a preferred architectural element for the biofilms of many environmental and host-dependent bacterial species alike.[3,4] Because of these properties and its low antigenic potential, cellulose secretion is key to the ecological success and host tissue colonization of both symbiotic and pathogenic bacteria that live in close association with plants and can thus have significant economic impact as biocontrol microorganisms, cellulose superproducers of biotechnological interest, or detrimental agricultural pathogens.[3,5] Examples include species from the *Gluconacetobacter* lineage as industrially relevant sources of crystalline bacterial cellulose (BC); multihost plant pathogens, such as *Dickeya dadantii*; human and animal enterobacterial pathogens, which can be transmitted through plant foods (e.g., *Escherichia coli*); biocontrol microorganisms, such as *Pseudomonas fluorescens* SBW25; and drought-resistance-promoting plant endophytes, such as *Enterobacter* sp. 638.[3,4]

BC secretion is determined by several types of dedicated *bcs* gene clusters, whose coordinated expression and downstream protein-protein interactions secure the assembly of multicomponent biosynthetic platforms that provide the physical conduit, protection, and energetics for the secretion of hydrophilic cellulosic polymers through the complex bacterial envelope.[3,4] The core Bcs components include the cyclic diguanylate (c-di-GMP)-activatable BcsAB synthase tandem that secures processive glucose polymerization and inner-membrane extrusion and, in gram-negative bacteria, the outer-membrane BcsC porin, whose periplasmic tetratricopeptide repeats likely serve as peptidoglycan-binding scaffolding motifs.[3,6]

In addition to these, multiple accessory subunits can play essential or regulatory roles in Bcs secretion system assembly, c-di-GMP sensing, subcellular synthase arraying, or covalent

modifications of the secreted polysaccharide (e.g., phosphoethanolamine [pEtN-] addition or cellulose acetylation).[3] The secreted homopolymer can thus feature additional chemical moieties likely contributing to interactions with other extracellular matrix components or present various degrees of crystallinity, where individual cellulose chains pack parallelly into higher-order cellulosic assemblies (e.g., cellulose microfibrils, ribbons, or sheets) via a combination of lateral hydrogen bonding and hydrophobic van der Waals interactions.[3] Together, bacterial synthase terminal complexes (TCs) can be thus viewed as multicomponent secretion systems yielding polymers with diverse physicochemical properties and roles in bacteria-host interactions.[3]

We demonstrated recently that in *Escherichia coli*, the BcsA synthase together with a periplasmic crown of BcsB protomers assembles into a stable, megadalton-sized secretory macrocomplex with four accessory subunits, which either enhance (BcsE and BcsF) or are essential for (BcsR and BcsQ) cellulose secretion.[7,8] Of these, BcsE is a degenerate GGDEF domain-containing protein, which provides a second c-di-GMP-sensing module in addition to the synthase's C-terminal PilZ domain ($BcsA^{PilZ}$) and is recruited to the inner membrane via interactions with BcsF, a single-pass transmembrane protein.[9] BcsR and BcsQ are a short polypeptide and a single-domain P-loop ATPase, respectively, which stabilize each other to form an atypical ATPase tandem with structural homology to membrane protein sortases. It has been proposed to participate in both secretion system assembly and—through direct interactions with BcsE—in synthase-proximal c-di-GMP enrichment for processive BcsA activation.[8,9] Finally, a yet distinct Bcs subunit, BcsG, was shown to covalently decorate the *E. coli* biomatrix cellulose with pEtN residues in the periplasm, most likely via transient interactions with the secretion macrocomplex.[3,10]

Despite strong conservation of the BcsAB tandem across species, in the economically relevant BC superproducer *Gluconacetobacter hansenii*, cellulose is secreted in a drastically different manner: a longitudinal nanoarray of synthase TCs assembles the individually extruded polysaccharide strands into a crystalline cellulose ribbon (CR) with implications in cell motility, flotation, and substrate colonization.[3,11] Crystalline BC secretion is dependent on two accessory subunits earlier proposed to interact in the periplasm: BcsD, a donut-shaped octamer with four luminal passageways thought to guide and prevent aggregation of the nascent polysaccharide, and BcsH, proposed as a short, 8-kDa-peptide-mediating linear BcsD arrangement in the periplasm necessary for crystalline ribbon formation.[12,13] However, we were recently able to provide the first atomic-resolution insights BcsHD-mediated BC crystallinity.[14] We showed that BcsH is in fact a proline-rich 37-kDa protein, which drives the oligomerization of BcsD octamers into a three-dimensional supramolecular scaffold.[14] We showed that, *in situ*, the BcsHD assemblies share remarkable morphological similarities with the recently discovered cytosolic "cortical belt," namely, an intracellular cytoskeletal element that spatially correlates with the cellulose exit sites and the assembled crystalline CR.[11,14] Finally, we detected specific protein-protein interactions between the BcsHD components and the regulatory $BcsA^{PilZ}$ module in the cytosol, further supporting that BcsHD feature an unexpected intracellular localization for inside-out control of TC array formation, similar to the tethering of membrane-embedded cellulose synthase complexes by cortical microtubules in plants (Figure S1).[11,14]

Interestingly, while *bcsH* has been postulated as specific for the *Gluconacetobacter* lineage, *bcsD* homologs are widespread across the proteobacterial clade, including in beneficial or harmful bacteria that live in close association with eukaryotic hosts (Figure 1A).[4] These encompass both symbionts and pathogens with clusters for the secretion of amorphous or semi-crystalline non-modified cellulose, as well as multiple species featuring *E. coli*-like genes for c-di-GMP enrichment and pEtN addition or *P. fluorescens* SBW25-like multicomponent clusters for cellulose acetylation (Figures 1A, S1A, and S2). Here, we examine the distribution of *bcsD* and its gene neighborhoods across Proteobacteria, present the structures and interactions of BcsD homologs from beneficial and pathogenic bacteria from the β- and γ-proteobacterial clades, determine key roles for the protein and its partners in the secretion of non-crystalline cellulose, and uncover commonalities and idiosyncrasies in the assembly and function of a diverse range of Bcs secretion systems.

RESULTS AND DISCUSSION

Proteobacterial *bcsD* and model organisms

BC synthesis is almost invariably carried out by a membrane-embedded BcsAB synthase/co-polymerase tandem; however, secretion of the polymer depends on the co-expression and assembly of multiple additional subunits.[3,4] Depending on these, three prevalent Bcs secretion systems have been proposed: type I, featuring *bcsD* as a hallmark gene in their *bcs* gene cluster(s) and so far studied in the *Gluconacetobacter* lineage, type II or *E. coli*-like, characterized by the presence of *bcsE* and *bcsG* homologs, and type III lacking all three of the above components.[3,4] Nevertheless, *bcs* clusters typically feature high mosaicity and hybrid architectures are not uncommon. Homologs of *bcsD* encoding the PF03500 family of proteins (protein families database PFAM) are thus found across the proteobacterial clade, including in many enterobacteria with adjacent *bcsEFG* operons similar to that of *E. coli* or in *Burkholderiales* with pseudomonad alginate-like clusters for cellulose acetylation (Figures 1A, S1A, and S2).[4,18] Interestingly, although the longest studied *Gluconacetobacter hansenii* (formerly *Acetobacter xylinum* and also known as *Komagataeibacter* or *Novacetimonas hansenii*) does not feature a homolog of the BcsQ ATPase, most *bcsD*-carrying clusters encode both the sortase-like ATPase and a proline-rich protein, such as BcsH-like homologs in α-, BcsP in β-, and BcsO in γ-Proteobacteria (Figure S2).[4,18]

To further unravel the roles of BcsD and its intraoperon partners, we focused on three model plant-colonizing microorganisms, which represent a diverse set of bacterial physiologies and secreted polysaccharides (Figure 1B). We establish here *Orrella dioscoreae*—a hereditary, endophytic symbiont of the wild yam *Dioscorea sansibarensis*—as a model organism for acetylated cellulose secretion from the β-proteobacterial clade.[19,20] We selected *Dickeya dadantii*—a multi-host, multi-organ γ-proteobacterial pathogen that causes soft-rot disease in economically relevant agricultural crops worldwide and secretes relatively thick but not crystalline cellulose

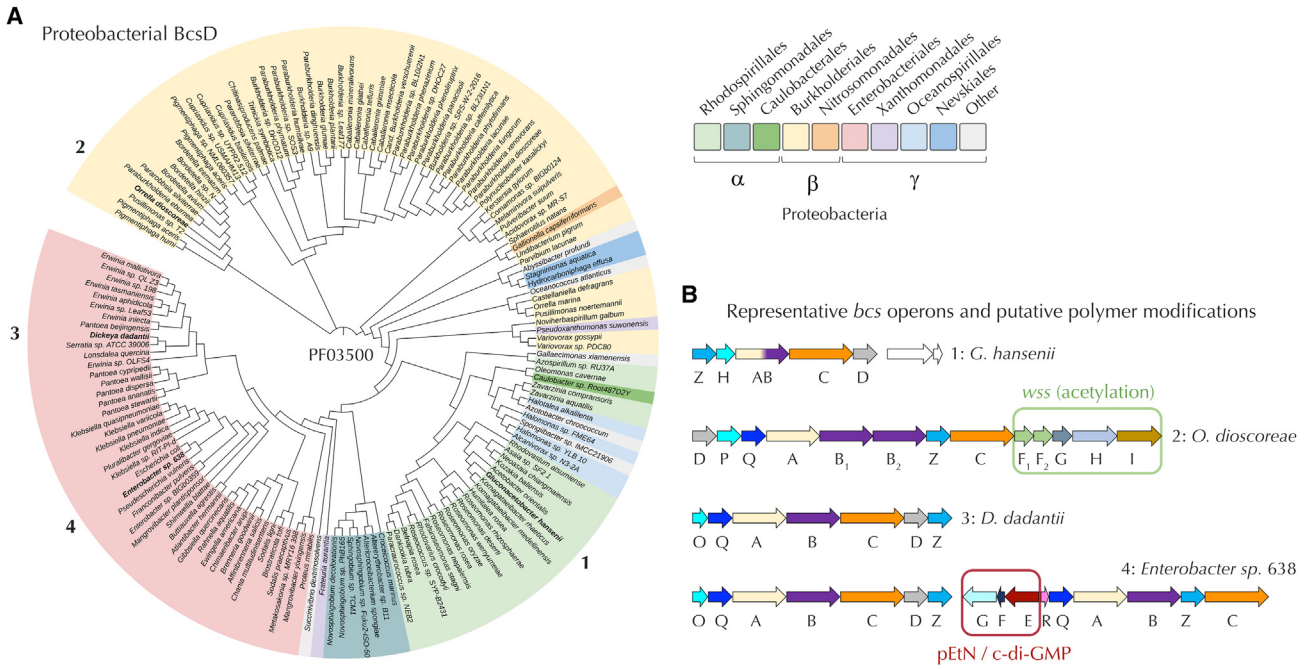

Figure 1. Proteobacterial BcsD

(A) Phylogenetic tree of representative α-, β-, and γ-proteobacterial BcsD sequences from the PFAM database (domain identifier PF03500). Plotted with iTOL.[15]

(B) Representative *bcs* operons and putative polymer modifications as found in (1) *Gluconacetobacter hansenii* (non-pathogenic, spoilage α-proteobacterium characterized by crystalline cellulose secretion), (2) *Orrella dioscoreae* (endosymbiotic β-proteobacterium carrying a *wss* cellulose acetylation cluster), (3) *Dickeya dadantii* (multi-host plant pathogen secreting semi-crystalline cellulose nanofibers),[16] (4) *Enterobacter* sp. 638 (isolated as poplar endophyte, multi-host plant growth-promoting microorganism,[17] carrying a *bcsEFG* cluster for synthase-proximal c-di-GMP enrichment [via BcsEF][8,9] and phosphoethanolamine-modified cellulose [via BcsG]).[10]

See also Figures S1 and S2.

nanofibers[16]—as a model for non-modified cellulose secretion. And finally, the plant growth- and drought-resistance-promoting *Enterobacter* sp. 638—which features three adjacent *bcs* operons, including an *E. coli*-like *bcsEFG* cluster—was chosen as a beneficial, economically relevant model that could provide insights into pEtN-modified cellulose production.[4,17,21]

O. dioscoreae as a model system and roles of BcsD in non-crystalline cellulose secretion

Several plant species establish specific symbioses with bacteria within their aerial organs. Leaf nodules or glands hosting symbiotic bacteria are present in diverse taxa, including dicots (several genera within the families Rubiaceae and Primulaceae) and monocots (*Dioscorea*).[20,22] Transmission of the symbiotic bacteria occurs through seeds and propagules: a colony of bacteria is present at the shoot apex and is thought to enable colonization of leaves and reproductive organs as the tissue develops.[20,22] Leaf nodule symbiosis in Primulaceae and Rubiaceae is obligate: seeds cured of the symbiotic *Burkholderia* bacteria by antibiotic or heat treatment germinate but do not develop past the seedling stage, and the symbiotic bacteria have so far escaped cultivation.[23] Contrary to other leaf symbionts, *Orrella dioscoreae* is an exclusive symbiotic bacteria colonizing leaf glands in the wild yam *Dioscorea sansibarensis* (Figure 2A) that can be isolated and cultured on standard microbiological media.[24] In addition, we recently adapted experimental tools for the both the manipulation of the *Orrella dioscoreae* genome and the cultivation of aposymbiotic plants in the laboratory.[20]

The *Orrella* genome features an interesting cluster linked to cellulose secretion that features genes coding for the regulatory BcsDPQ subunits mentioned above, genes for the $BcsAB_1B_2ZC$ core components for cellulose synthesis and periplasmic export, and a $wssF_1F_2GHI$ cluster potentially involved in cellulose acetylation (Figure 1B). BC secretion has traditionally been viewed as important for survival in harsh environments and initial attachment to eukaryotic or abiotic surfaces,[3,26] however, the life cycles of leaf endosymbionts, including *O. dioscoreae*, entirely depend on and develop within their plant hosts. Moreover, preserved operons for BC biosynthesis have been detected even in the reduced genomes of some *Candidatus* Paraburkholderia species that are obligate leaf endophytes of *Vangueria* and other Rubiaceae, suggesting that the biosynthetic process of BC secretion has been maintained throughout millions of years of evolution *in planta*.[23] Using comparative RNA sequencing (RNA-seq), we showed previously that the *bcs-wss* operon of *Orrella* is overexpressed *in planta* compared with cultures, suggesting a role in interactions with the host.[19] This is especially surprising as *Orrella* does not utilize sugar-based carbon sources,[24] likely making cellulose secretion entirely gluconeogenesis dependent and hence energetically costly, whereas the obligate endosymbiosis places environmental survival, initial attachment to the host and horizontal transmission under lesser evolutionary

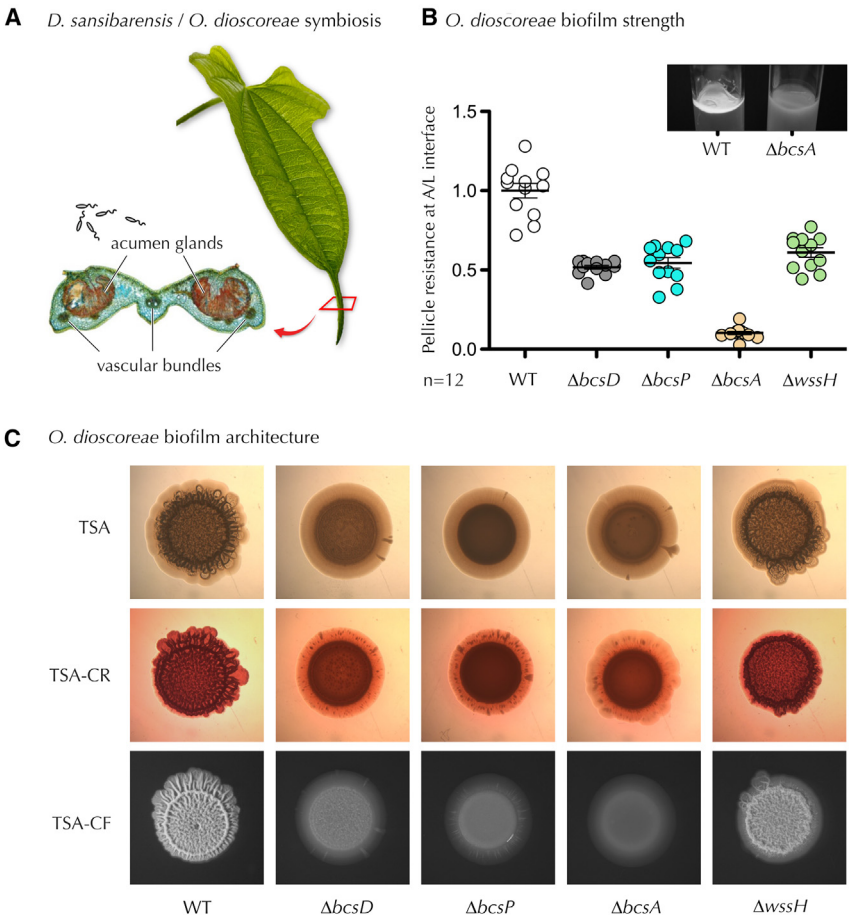

Figure 2. Beyond crystalline cellulose secretion: Roles of *O. dioscoreae* BcsD in biofilm strength and architecture

(A) Schematic of the *Orrella dioscoreae*—*Dioscorea sansibarensis* leaf symbiosis: a juvenile plant leaf and a cross-section of a leaf acumen are shown. The bacteria colonize as endosymbiotic, monospecies biofilms the acumen glands, around which several vascular bundles can be found.[20]

(B and C) Role of cellulose and putative modifications in *O. dioscoreae* biofilms: (B) Biofilm strength of wild-type *O. dioscoreae* relative to *bcs* and *wss* mutants shown as the mass of glass microbeads sufficient to break through the cellulosic pellicle formed at the air-liquid interface (ALI).[25] Shown are the results (mean and standard error of the mean) of 12 independent replicates for each strain (n = 12), normalized to wild type (WT). Top right inset, example ALI of wild-type and Δ*bcsA O. dioscoreae* grown for 4 days in calcofluor-supplemented tryptic soy broth (TSB).

(C) Colony morphologies, Congo red (CR) binding and calcofluor (CF) fluorescence of *O. dioscoreae* variants grown on tryptic soy agar (TSA), TSA-CR, and TSA-CF for 4 days at 30°C.

See also Figure S3.

pressure. Given the availability of genetic and bacteria/plant cultivation tools, we thus propose that—similar to the *Vibrio*-squid symbiosis in quorum sensing research[27,28]—the *Orrella* - *Dioscorea* system can provide a straightforward binary system to examine the roles of BC secretion and acetylation *in planta* without the interference of a complex host microbiome.

To experimentally test for roles of cellulose secretion in *Orrella* physiology and biofilm formation, we adapted genetic tools recently developed for *Pseudomonas* spp. and generated non-polar, in-frame deletion mutants of *O. dioscoreae* for the *bcsA*, *bcsD*, *bcsP*, and *wssH* genes, the latter encoding a putative membrane-bound O-acetyl transferase for cellulose acetylation (Figures 2 and S1). In static liquid cultures, *O. dioscoreae* grows primarily as a calcofluor-binding pellicle at the air-liquid interface (ALI), suggesting active cellulose secretion that likely aids flotation and surface biofilm cohesion (Figure 2B, inset). In support of this, the Δ*bcsA* mutant, which lacks a functional cellulose synthase, showed significant turbidity throughout the culture volume and the virtual lack of a calcofluor-enriched ALI pellicle (Figures 2B, inset and S3). Having established a phenotypic manifestation of cellulose secretion, we next proceeded to examine the strength of ALI biofilms in the above chromosomal mutants and in the absence of cellulose-binding stains that might affect the native polymer interactions. We measured the strength of ALI pellicles as the mass of glass microbeads necessary to break through the static culture surface (biofilm breaking mass, relative to wild type)[25] and observed that each of the Δ*bcsD*, Δ*bcsP*, and Δ*wssH* mutants features strongly reduced mechanical resistance (Figure 2B). Conversely, when grown on solid agar wild-type *Orrella dioscoreae* features very pronounced surface wrinkling and calcofluor binding, whereas the Δ*bcsA* mutant exhibits only background fluorescence (indicating that cellulose is likely the major calcofluor-binding matrix component) and a smooth colony morphotype (Figure 2C). Interestingly, although the Δ*bcsD*, Δ*bcsP*, and Δ*wssH* mutants feature comparable ALI strengths, they exhibit different propensities for calcofluor binding and different colony morphotypes (Figures 2C and S3). Of the three, Δ*wssH* showed mostly preserved wrinkling and calcofluor binding, indicating that cellulose acetylation is likely not required for cellulose synthesis and export but rather partakes in extracellular interactions for biofilm cohesion. In contrast, both the Δ*bcsD* and Δ*bcsP* mutants are strongly deficient in both calcofluor binding and surface wrinkling, with the latter presenting a virtually smooth colony morphotype. Together these data indicate that *Orrella dioscoreae* not only secretes biofilm-promoting cellulose but also that the synthesis, structure, and function of the secreted polysaccharide depend on the accessory BcsD and BcsP subunits, as well as on acetylation of the nascent polymer. To our knowledge, this is the first report of functional roles for a BcsD homolog and a proline-rich intraoperon partner in cellulose secretion, biofilm strength, and macrocolony architecture in non-crystalline cellulose-secreting bacteria.

Cryo-EM structure of ~68 kDa O. dioscoreae BcsD at 2.3 Å resolution

To examine the conservation of BcsD across species, we first proceeded to determine the structure of *O. dioscoreae* BcsD. Similar to its *G. hansenii* counterpart, *O. dioscoreae bcsD*

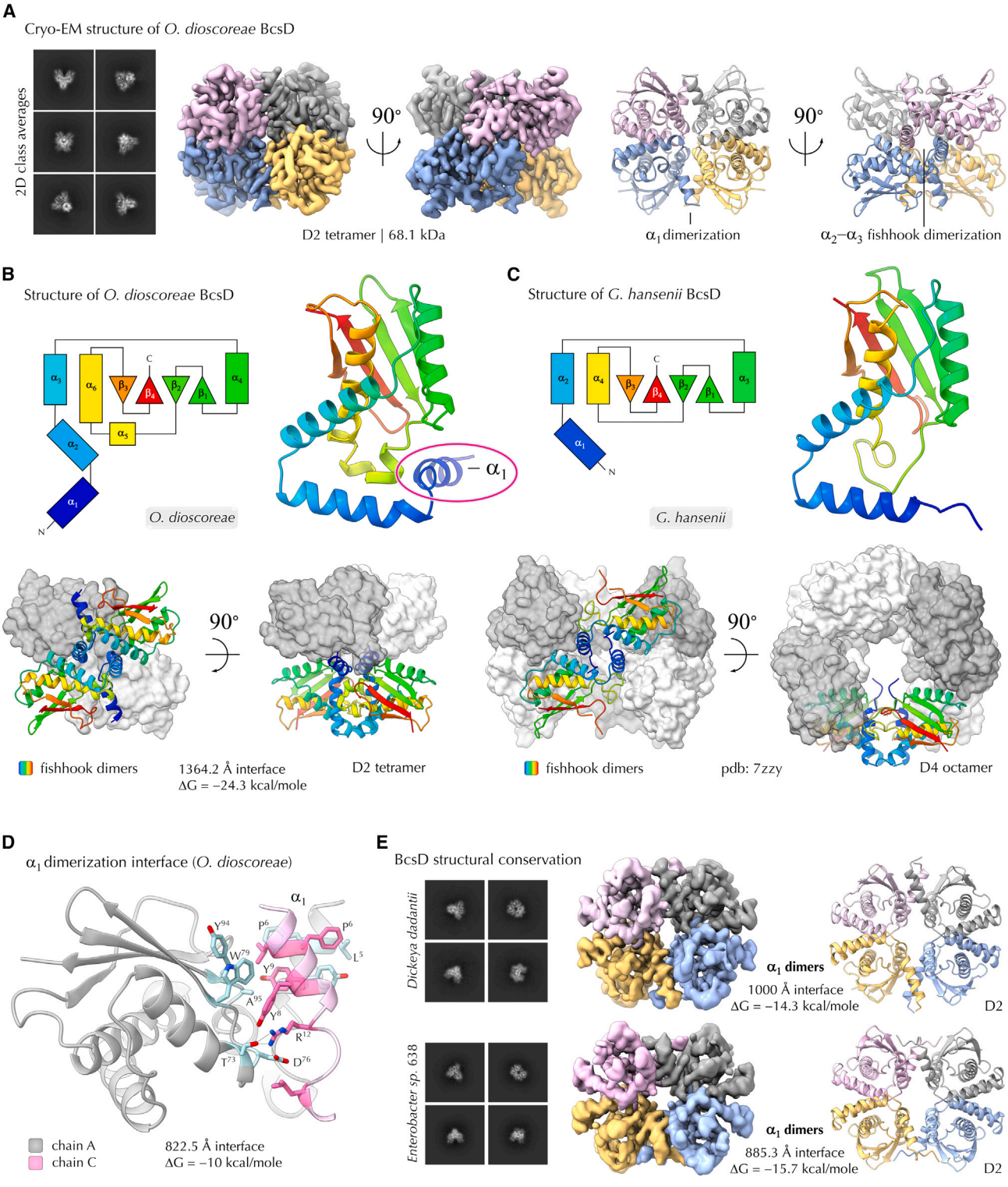

Figure 3. Structures of proteobacterial BcsD homologs

(A) Cryo-EM structure of *O. dioscoreae* BcsD: left, representative views (2D class averages) of BcsD$^{O.dioscoreae}$ molecules in solution. Middle, two orthogonal views of the BcsD$^{O.dioscoreae}$ electron density map, colored by subunits. Right, two orthogonal views of the BcsD$^{O.dioscoreae}$ atomic model shown in ribbon representation and colored by subunits.

(B and C) Comparison of the cryo-EM structures of BcsD from *O. dioscoreae* (B) and *G. hansenii* (C).[14] Clockwise for each protein: secondary structure topologies showing an additional N-terminal helix in *O. dioscoreae* BcsD (α_1); tertiary fold shown as rainbow-colored ribbons with N-termini in blue and C-termini in

(legend continued on next page)

encodes a relatively small, 17 kDa, protein. Because the purified protein failed to crystallize and based on the octameric state previously reported for *G. hansenii* BcsD,[12,14] we resorted to single-particle cryoelectron microscopy (cryo-EM) despite the very low molecular weight of the protein (Figure 3A). Surprisingly, rather than forming the characteristic for *Gluconacetobacter* donut-shaped octamers where the luminal part is separated into four independent passageways by the N-terminal tails of the individual subunits,[12,14] BcsD of *O. dioscoreae* assembled into D2-symmetric, tetrahedron-like tetramers (Figure 3A). Intersubunit contacts within the tetramer feature the fishhook-like dimerization interface also observed in *G. hansenii* BcsD, formed by mostly hydrophobic interactions between the interlocking α2 and α3 in the *O. dioscoreae* homolog and corresponding to α1 and α2 in *G. hansenii* BcsD. Each of these interfaces buries about 1,364 Å^2 from the overall surface and contributes a free energy gain of −24.3 kcal/mol to the assembly (Figures 3B, 3C, and S4A–S4D).[29]

Importantly, the *O. dioscoreae* BcsD protomer presents an overall α1-α2-α3-α4-β1-β2-α5-α6-β3-β4 topology (Figure 3B), which differs from its *Gluconacetobacter* counterpart (Figure 3C) primarily by the presence of an additional N-terminal α1 helix. *O. dioscoreae* BcsD and PF03500 members in general do not feature detectable signal/leader peptides,[14] and α1 makes extensive intra- and intersubunit contacts with the rest of the protein core, thus making it unlikely that this helix is removed in a post-translational cleavage event. In particular, the α1-helix guides the formation of a set of different dimerization interfaces within the tetramer, each of which buries about 822 Å^2 and contributes a free energy gain of −10 kcal/mol to the quaternary structure (Figure 3D).[29] α1 dimerization is primarily driven by symmetric hydrophobic contacts between adjoining α1-helices, as well as a combination of hydrophobic and polar interactions with the protein core of the neighboring subunit (e.g., R^{12} from each protomer partaking in polar contacts with T^{73} and D^{76} from its α1-symmetry mate and W^{79} and Y^{94}A contributing to the formation of a hydrophobic pocket for the N-proximal tip of the neighboring α1) (Figure 3D). Importantly, the purified *O. dioscoreae* BcsD purified as a single gaussian peak upon gel filtration and did not present additional higher-order oligomerization species within the studied cryo-EM samples, neither in terms of octamer formation nor in terms of inter-tetramer contacts (Figures 3A and S5A).

Cryo-EM structures of *D. dadantii* and *Enterobacter* sp. 638 BcsD and determinants of structural conservation across species

We next analyzed ~150 of the PF03500 family members,[31] and the AlphaFold-predicted structures[32] demonstrate that—apart from few organisms close to the slow-growing crystalline cellulose superproducer *G. hansenii*—the presence of an N-terminal α1-helical extension is likely a predominant feature across Proteobacteria (Data S1). To validate these findings, we cloned and purified the BcsD homologs from *D. dadantii*, a multihost plant pathogen secreting semi-crystalline non-modified cellulose, and *Enterobacter* sp. 638, a plant growth- and drought-resistance-promoting endophyte carrying an *E. coli*-like *bcsEFG* cluster. The cryo-EM structures for both proteins solved at ~4 Å resolution corroborate an *O. dioscoreae*-like tetrameric BcsD architecture, where intersubunit contacts are driven both by α2/α3 fishhook interlocks and by α1-driven dimerization, with the latter burying between 885 and 1,000 Å^2 surface area and contributing free energy gains between −14.3 and −15.7 kcal/mol to the quaternary structure assemblies (Figure 3E).[29] Together, these data suggest that the presence of an N-terminal hydrophobic helix in BcsD could be used as a predictor of the protein's oligomeric state and opens the potential for the engineering of BcsD variants with altered quaternary structure and, possibly, of fast-growing bacterial strains with increased propensity for crystalline cellulose secretion.

BcsP and BcsO: Proline-rich BcsD partners

We showed previously that in *G. hansenii* BcsD is driven into linear filaments via the C-terminal region of proline-rich intraoperon partner BcsH, whereas the latter's N-terminal region likely drives the higher-order assembly of BcsHD filaments into the so-called "cortical belt": a stacked cytoskeletal belt-like structure that runs along the long axis of the *G. hansenii* cell and parallel to the nascent CR (Figure S1B).[11,14] This surprising intracellular localization was further supported by protein interaction data, suggesting that the BcsHD scaffold interacts with the c-di-GMP-sensing BcsA^{PilZ} domains and thus might directly drive the longitudinal arrangement of synthase TCs for crystalline CR assembly.[14]

As mentioned above, despite the absence of *bona fide bcsH* homologs, most of the *bcsD*-positive clusters of β- and γ-Proteobacteria feature genes for proline-rich BcsP or BcsO proteins, as well as genes for the BcsQ ATPase that interacts directly with the BcsA synthase and is essential for cellulose secretion in *E. coli*, but is absent in the *Gluconacetobacter* lineage (Figure S2).[4,18] We therefore constructed split adenylate cyclase (AC) protein fusions to examine putative interactions between the regulatory BcsD, BcsP, BcsQ, and BcsA^{PilZ} modules based on *in cellulo* bacterial two-hybrid functional complementation (BACTH, Figure 4A).[33] The data show that BcsD and BcsP not only interact with each other but also with the BcsQ ATPase, which, in turn, interacts with the BcsA^{PilZ} domain. This corroborates an intracellular localization for the BcsD and BcsP partners and the formation of multi-component Bcs assemblies for cellulose secretion regulation.

red; quaternary structures showing preserved fishhook interprotomer contacts (see also Figures S4A–S4D and Hu et al.[12] and Abidi et al.[14]) but markedly different tetrameric (D2) vs. octameric (D4) assemblies.

(D) The α_1 dimerization interface driving tetrameric structure. The buried protomer-protomer interface and dimerization free energy gain were calculated in PDBePISA,[29] key residues are highlighted and shown in sticks. For simplicity only the N-terminal region of the second protomer is shown.

(E) Cryo-EM structures of enterobacterial BcsD homologs. From left to right, 2D class averages, cryo-EM density maps and cartoon representations of the refined tetrameric atomic models for BcsD from *D. dadantii* (top) and *Enterobacter* sp. 638 (bottom). The buried interfaces and free energy gains from α_1 dimerization in each structure were calculated in PDBePISA, as above. Map and model representations: ChimeraX.[30]

See also Figures S4A–S4D and Data S1.

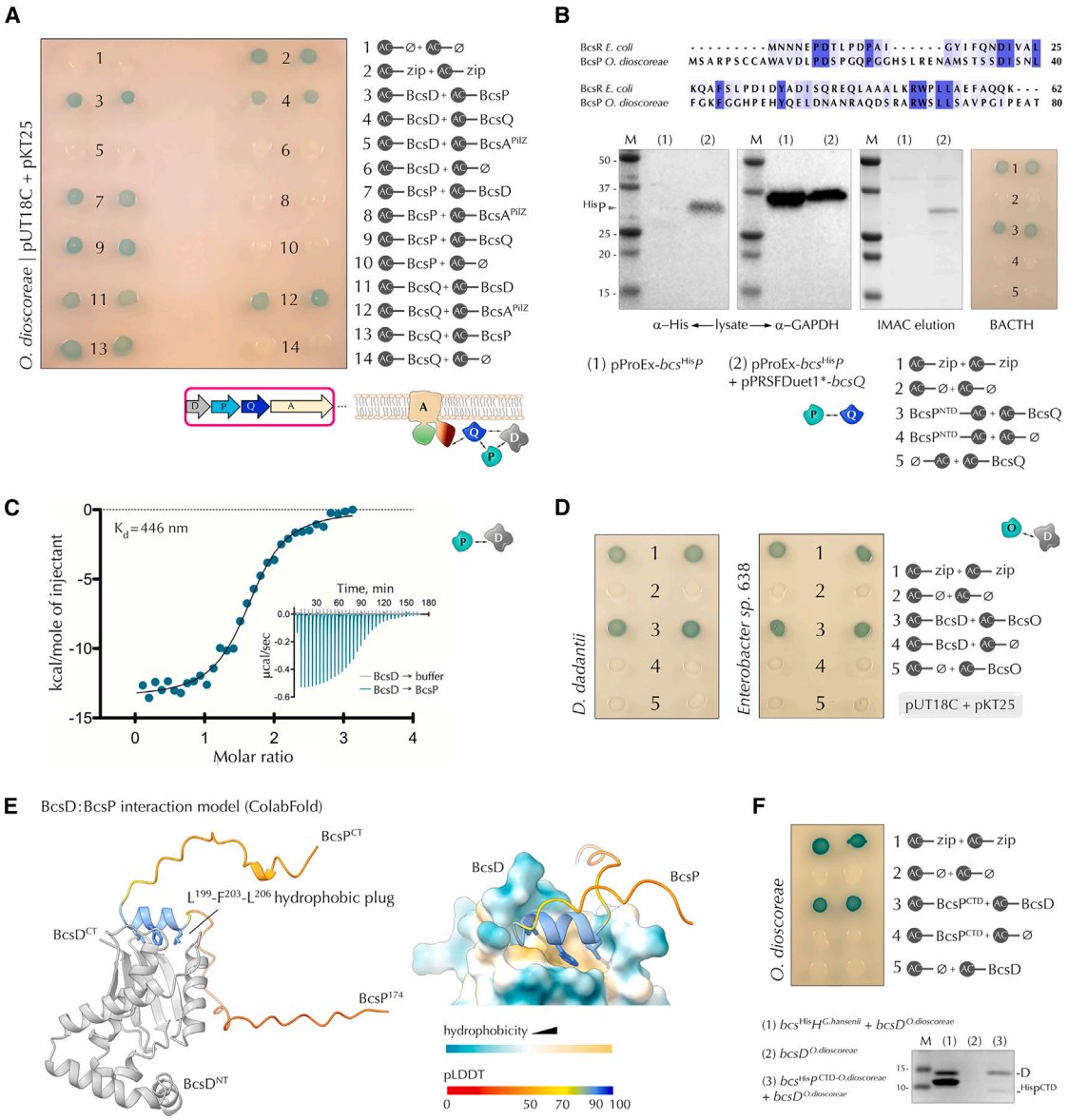

Figure 4. Regulatory subunit interactions in the *O. dioscoreae* Bcs secretion system

(A) Bacterial two-hybrid (BACTH) assay of interactions among regulatory Bcs subunits and the BcsA synthase (as BcsA^{PilZ}) based on split adenylate cyclase (AC) protein fusions and interaction-dependent functional reconstitution in a *cya*-deficient *E. coli* strain.[33,34] The positive zip/zip control is based on coexpressed AC fragments each fused to a homodimerizing leucine zipper region of the yeast protein GCN4. Interactions were evaluated by blue colony growth on X-gal-supplemented LB-agar plates. Co-transformations with unfused AC fragment-expressing vectors were used as negative controls.

(B) Similarities between PF10945 family members BcsR$^{E.coli}$ and BcsP$^{O.dioscoraee}$ BcsP. Top, sequence alignment between the BcsR and BcsP^{NTD}, colored by conservation. Bottom left, BcsP^{FL} expression in the absence and presence of co-expressed BcsQ (from pRSFDuet1*-*bcsQ*) from the same pProEx-Htb-*bcs*^{His}*P* expression vector. Glyceraldehyde-3-phosphate dehydrogenase (GAPDH) detection was used as loading control for the lysate fractions analyzed by western blot. Bottom right, bacterial two-hybrid assay of interactions between BcsP^{NTD} (in pUT18) and BcsQ (in pKT25); positive and negative controls as in (A).

(C) Isothermal titration calorimetry (ITC) profile of the BcsD to BcsP titration. Titration of BcsD into buffer was used to account for dilution heat effects and subtracted from the calculation of the apparent dissociation constant (446 nM) and stoichiometry of interaction (~1.7).

(D) Bacterial two-hybrid assay of interactions between BcsD and BcsO homologs from *D. dadantii* and *Enterobacter* sp. 638.

(E) ColabFold prediction of BcsP binding to a hydrophobic intrasubunit pocket on BcsD (pLDDT: predicted local distance difference test score; NT: N-terminus; CT: C-terminus). Left, BcsD is colored in grey, BcsP C-terminal region is colored by the pLDDT. Right, zoom-in of the intersubunit contacts: the hydrophobic plug residues of BcsP, colored by pLDDT, are shown as sticks; BcsD is shown in surface and colored by hydrophobicity in a teal-to-gold gradient.

(F) Experimental validation of the BcsP-BcsD interaction. Top, bacterial two-hybrid assay of interactions between BcsP^{CTD} (in pUT18C) and BcsD (in pKT25); positive and negative controls as above. Bottom, IMAC co-purification of BcsD via Bcs^{His}P^{CTD}. Lysates with co-expressed Bcs^{His}H$^{CTD\text{-}G.hansenii}$ (from pProEx-Htb) and BcsD$^{O.dioscoreae}$ (from pRSFDuet1*) or BcsD$^{O.dioscoreae}$ (from pRSFDuet1*) alone were also subjected to IMAC purification as positive and negative controls, respectively.

See also Figure S4E.

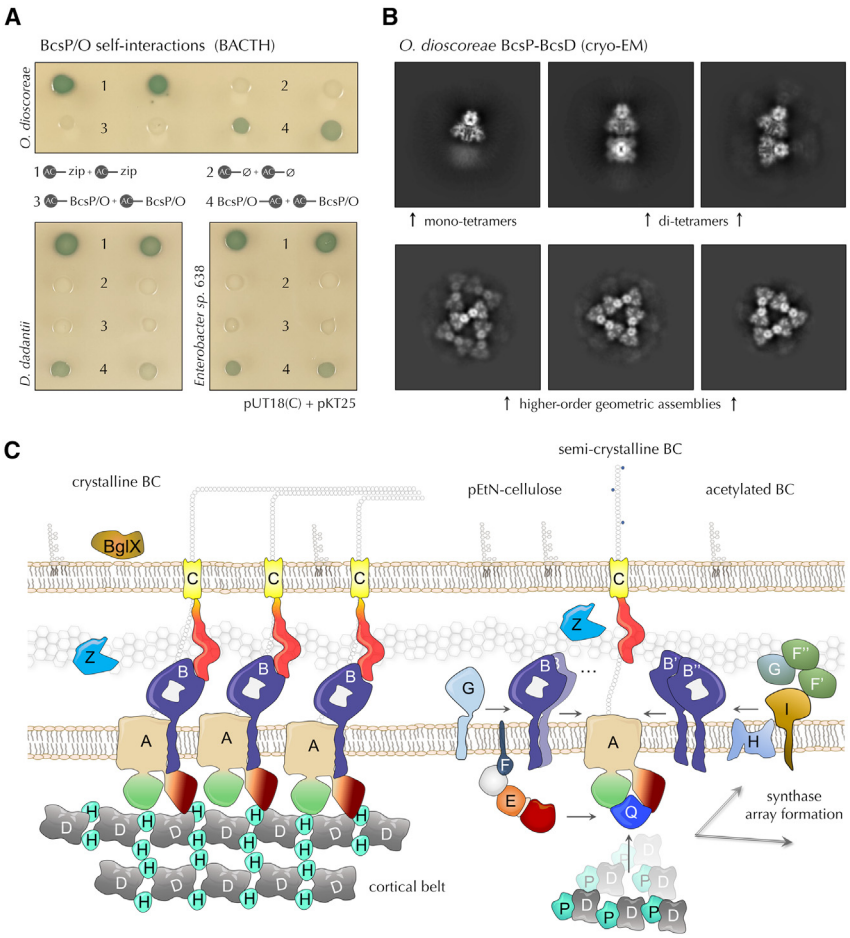

Figure 5. Higher order interactions and proposed mechanism for BcsH/P/O-BcsD scaffolds for cellulose secretion assembly across the proteobacterial clade

(A) Bacterial two-hybrid assay of interactions between $BcsP^{FL}$ or $BcsO^{FL}$ subunits.

(B) Cryo-EM 2D class averages of *O. dioscoreae* BcsD-BcsP assemblies showing stable organization of di-tetrameric and higher-order geometric assemblies in solution, not observed in the BcsD-only datasets.

(C) Proposed roles of BcsH/P/O-BcsD intracellular scaffolds in synthase nanoarray formation for the secretion of crystalline (*G. hansenii*, left) or amorphous (e.g., acetylated [*O. dioscoreae*], semi-crystalline [*D. dadantii*], or pEtN-modified [*Enterobacter* sp. 638-like]) bacterial cellulose.

Interestingly, the N-terminal regions of BcsP homologs are similar to the BcsR cellulose secretion regulator and have been assigned to the same PFAM domain (PF10945; Figure 4B, top).[4,31] Although often missed in genome annotations in the past, BcsR peptides are widespread across enterobacterial Bcs secretion systems and, at least in *E. coli*, BcsR and BcsQ mutually stabilize each other, interact directly with the synthase, regulate its integrity in the membrane and catalytic activity, and are essential for cellulose secretion.[3] Indeed, similar to $BcsR^{E.\ coli}$,[9] *O. dioscoreae* BcsP could be heterologously expressed only in the presence of BcsQ and BACTH assays indicate direct interactions between the ATPase and the N-terminal region of its proline-rich partner (Figure 4B, bottom). Overall, however, both BcsP and BcsO are predicted to adopt a disordered tertiary structure similar to that of *G. hansenii* BcsH, likely due to the high percentage of proline and other small neutral amino acids in their primary structures (Figure S4E).[14,32] This led us to the hypothesis that BcsP and BcsO can further act as β- and γ-proteobacterial counterparts to *Gluconacetobacter* BcsH. Indeed, isothermal titration calorimetry experiments corroborated direct and high-affinity interactions between *O. dioscoreae* BcsD and BcsP (Figure 4C) and bacterial two-hybrid assays confirmed interactions between *D. dadantii* and *Enterobacter* sp. 638 BcsD and BcsO (Figure 4D). Similar to *G. hansenii* BcsH,[14] BcsP is predicted to interact with BcsD via hydrophobic interactions between a short, C-proximal helix in BcsP featuring an L^{199}-F^{203}-L^{206} hydrophobic "plug" and an intrasubunit pocket between BcsD's central β-sheet and helices α4 and α6 (Figure 4E). Conversely, we show that *O. dioscoreae* $BcsP^{CTD}$ interacts directly with BcsD *in cellulo*, by both bacterial two-hybrid interaction assays and via heterologous co-expression and immobilized metal affinity chromatography (IMAC) purification (Figure 4F).

Higher-order BcsP/O-BcsD cytoskeletal assemblies for proteobacterial BC secretion

We recently showed that what determines the functional roles of *G. hansenii* BcsH in cellulose secretion is not its interaction with BcsD per se but rather the ability of the protein to drive BcsD filamentation and cortical belt assembly.[14] We therefore examined whether BcsP could play similar roles in the formation of regulatory cytoskeletal assemblies. Using bacterial two-hybrid complementation assays we show that *O. dioscoreae* BcsP and *D. dadantii* and *Enterobacter* sp. 638 BcsO can partake in self-oligomerization interactions (Figure 5A) and possibly recruit BcsD tetramers into higher-order intracellular structures. To examine this hypothesis further, we visualized reconstituted BcsD-BcsP assemblies by cryo-EM (Figure 5B). Although the particle distribution featured preferential orientation and prevented us from resolving the three-dimensional structure of the BcsD-BcsP complexes, particle 2D classification clearly revealed the formation of both BcsP-driven dimers of BcsD tetramers and higher-order geometric assemblies (Figure 5B). Notably, whereas the *G. hansenii* BcsHD assemblies feature filamentous architecture with BcsD donut-shaped octamers adopting $BcsH^{CTD}$-driven beads-on-a-string arrangements that stack into the cortical belt to assemble a narrow longitudinal array of synthase TCs *in cellulo*,[14] the herein observed *O. dioscoreae* BcsPD arrays feature triangular tiling modules likely determined by the tetrahedron-like quaternary structure of the individual BcsD tetramers. This tiled architecture could provide a modular platform for the subcellular recruitment of not only the catalytic Bcs core and

secretion of thicker, multistrand cellulose fibrils (as proposed for *D. dadantii*, for example)[16] but also of polymer modification complexes for pEtN addition or cellulose acetylation, environment-sensing partners for switch between free-living and host-associated life-styles, and activating diguanylate cyclases for localized c-di-GMP enrichment. The exact molecular mechanisms of how and where these Bcs clusters arrange in the cell to secure the secretion of system-specific cellulosic polymers remain to be further examined.

Together, we herein examine the distribution, structure, interactions, and function of the BcsD subunit as an intracellular scaffold component for cellulose synthesis across Proteobacteria. Using targeted mutagenesis and phenotypic assays of biofilm formation in *O. dioscoreae*, we establish the species as a model organism for BC secretion and acetylation that, together with its plant host, holds promise for deciphering additional roles of BC secretion *in planta*. We further demonstrate for the first time roles for a BcsD homolog in cellulose secretion and biofilm strength and architecture in non-crystalline cellulose-secreting bacteria. Using single-particle cryo-EM, we demonstrate that, unlike $BcsD^{G.hansenii}$, which assembles into donut-shaped octamers, the three low-molecular-weight BcsD homologs studied here form D2-symmetric, tetrahedron-like tetramers. We further determine that this quaternary structure assembly is driven by the presence of an N-terminal α-helical extension (α1), which is likely conserved in the majority of *bcsD*-encoding β- and γ-Proteobacteria. We also show that, despite the absence of *bcsH* homologs per se, most of the examined *bcs* clusters of β- and γ-Proteobacteria feature genes for proline-rich BcsP/O proteins, which self-oligomerize and interact with their intraoperon BcsD partners to drive higher-order geometric BcsP/O-BcsD assemblies, visualized by cryo-EM. We further demonstrate that BcsP acts as a BcsR-BcsH hybrid protein and that the BcsPD partners also interact with the regulatory ATPase BcsQ and, through the latter, with the BcsA synthase. Together, our data suggest that BcsD and its proline-rich partners can form diverse cytoskeletal scaffolds throughout the proteobacterial clade, which likely determine synthase array formation and interactions, exopolysaccharide secretion and modifications, and the resultant biofilm strength and architecture in a large variety of microbial species. Future work combining genetic, phenotypic, and correlative imaging approaches is necessary to visualize the subcellular organization of these structures *in situ*, as well as their assembly and roles *in planta*. The results presented here not only shed light into a prevalent biosynthetic process beyond a single bacterial lineage but can also be harnessed for the biotechnological production of tailored exopolysaccharides with different degrees of crystallinity or chemical modifications, for improving prevention strategies against plant diseases, and for the engineering of pathogen-displacing, plant growth- and/or drought-resistance-promoting biocontrol organisms of agricultural and environmental interest.

STAR★METHODS

Detailed methods are provided in the online version of this paper and include the following:

SUPPLEMENTAL INFORMATION

Supplemental information can be found online at https://doi.org/10.1016/j.cub.2023.11.057.

ACKNOWLEDGMENTS

This project received funding from the ERC Executive Agency under grant agreement 757507-BioMatrix-ERC-2017-StG (to P.V.K.) and was also supported by the IECB, the CNRS, a Université de Bordeaux IDEX Junior Chair grant ExoPol (to P.V.K.), and an ERASMUS+ Intern Traineeship Program (to A.N.). The work has also supported and has benefited from the IECB cryo-EM platform, and the authors acknowledge the European Synchrotron Radiation Facility (ESRF, France) for data collection at the CM01 beamline in Grenoble. We are grateful to all current and former members of the SBB group and especially to Lucía Torres-Sanchez and Axel Siroy for technical assistance in student training and data pre-processing. Finally, we would like to thank Dr. William Nicolas, Dr. Erwan Gueguen, and Dr. Sophie Bleves for gifts of strains and plasmids and for stimulating discussions on cellulose synthesis (W.N.).

AUTHOR CONTRIBUTIONS

P.V.K. conceived the project. P.V.K. and T.G.S. designed the experimental procedures. P.V.K., T.G.S., A.N., and L.P. performed and optimized the experiments and analyzed the data. M.D. assisted in cryo-EM sample preparation, grid screening, and data collection (Talos Arctica, IECB). S.M. and A.C. designed initial protocols for the engineering of *O. dioscoreae* scarless deletion mutants. P.V.K. wrote the paper with significant contributions from T.G.S. and A.C.

DECLARATION OF INTERESTS

The authors declare no competing interests.

Received: October 17, 2023
Revised: November 20, 2023
Accepted: November 27, 2023
Published: December 22, 2023

REFERENCES

1. O'Toole, G., Kaplan, H.B., and Kolter, R. (2000). Biofilm formation as microbial development. Annu. Rev. Microbiol. *54*, 49–79.

2. Flemming, H.C., Wingender, J., Szewzyk, U., Steinberg, P., Rice, S.A., and Kjelleberg, S. (2016). Biofilms: an emergent form of bacterial life. Nat. Rev. Microbiol. *14*, 563–575.

3. Abidi, W., Torres-Sánchez, L., Siroy, A., and Krasteva, P.V. (2022). Weaving of bacterial cellulose by the Bcs secretion systems. FEMS Microbiol. Rev. *46*, fuab051.

4. Römling, U., and Galperin, M.Y. (2015). Bacterial cellulose biosynthesis: diversity of operons, subunits, products, and functions. Trends Microbiol. *23*, 545–557.

5. Yaron, S., and Römling, U. (2014). Biofilm formation by enteric pathogens and its role in plant colonization and persistence. Microb. Biotechnol. *7*, 496–516.

6. McNamara, J.T., Morgan, J.L.W., and Zimmer, J. (2015). A molecular description of cellulose biosynthesis. Annu. Rev. Biochem. *84*, 895–921.

7. Krasteva, P.V., Bernal-Bayard, J., Travier, L., Martin, F.A., Kaminski, P.A., Karimova, G., Fronzes, R., and Ghigo, J.M. (2017). Insights into the structure and assembly of a bacterial cellulose secretion system. Nat. Commun. *8*, 2065.

8. Abidi, W., Zouhir, S., Caleechurn, M., Roche, S., and Krasteva, P.V. (2021). Architecture and regulation of an enterobacterial cellulose secretion system. Sci. Adv. *7*, eabd8049.

9. Zouhir, S., Abidi, W., Caleechurn, M., and Krasteva, P.V. (2020). Structure and multitasking of the c-di-GMP-sensing cellulose secretion regulator BcsE. mBio *11*, e01303-20.

10. Thongsomboon, W., Serra, D.O., Possling, A., Hadjineophytou, C., Hengge, R., and Cegelski, L. (2018). Phosphoethanolamine cellulose: a naturally produced chemically modified cellulose. Science *359*, 334–338.

11. Nicolas, W.J., Ghosal, D., Tocheva, E.I., Meyerowitz, E.M., and Jensen, G.J. (2021). Structure of the bacterial cellulose ribbon and its assembly-guiding cytoskeleton by electron cryotomography. J. Bacteriol. *203*, e00371-20.

12. Hu, S.Q., Gao, Y.G., Tajima, K., Sunagawa, N., Zhou, Y., Kawano, S., Fujiwara, T., Yoda, T., Shimura, D., Satoh, Y., et al. (2010). Structure of bacterial cellulose synthase subunit D octamer with four inner passageways. Proc. Natl. Acad. Sci. USA *107*, 17957–17961.

13. Sunagawa, N., Fujiwara, T., Yoda, T., Kawano, S., Satoh, Y., Yao, M., Tajima, K., and Dairi, T. (2013). Cellulose complementing factor (Ccp) is a new member of the cellulose synthase complex (terminal complex) in *Acetobacter xylinum*. J. Biosci. Bioeng. *115*, 607–612.

14. Abidi, W., Decossas, M., Torres-Sánchez, L., Puygrenier, L., Létoffé, S., Ghigo, J.M., and Krasteva, P.V. (2022). Bacterial crystalline cellulose secretion via a supramolecular BcsHD scaffold. Sci. Adv. *8*, eadd1170.

15. Letunic, I., and Bork, P. (2021). Interactive Tree Of Life (iTOL) v5: an online tool for phylogenetic tree display and annotation. Nucleic Acids Res. *49*, W293–W296.

16. Jahn, C.E., Selimi, D.A., Barak, J.D., and Charkowski, A.O. (2011). The Dickeya dadantii biofilm matrix consists of cellulose nanofibres, and is an emergent property dependent upon the type III secretion system and the cellulose synthesis operon. Microbiology (Reading) *157*, 2733–2744.

17. Taghavi, S., van der Lelie, D., Hoffman, A., Zhang, Y.B., Walla, M.D., Vangronsveld, J., Newman, L., and Monchy, S. (2010). Genome sequence of the plant growth promoting endophytic bacterium *Enterobacter sp.* 638. PLoS Genet. *6*, e1000943.

18. Saha, C.K., Sanches Pires, R., Brolin, H., Delannoy, M., and Atkinson, G.C. (2021). FlaGs and webFlaGs: discovering novel biology through the analysis of gene neighbourhood conservation. Bioinformatics *37*, 1312–1314.

19. De Meyer, F., Danneels, B., Acar, T., Rasolomampianina, R., Rajaonah, M.T., Jeannoda, V., and Carlier, A. (2019). Adaptations and evolution of a heritable leaf nodule symbiosis between *Dioscorea sansibarensis* and *Orrella dioscoreae*. ISME J. *13*, 1831–1844.

20. Acar, T., Moreau, S., Coen, O., De Meyer, F., Leroux, O., Beaumel, M., Wilkin, P., and Carlier, A. (2022). Motility-independent vertical transmission of bacteria in leaf symbiosis. mBio *13*, e0103322.

21. Taghavi, S., Wu, X., Ouyang, L., Zhang, Y.B., Stadler, A., McCorkle, S., Zhu, W., Maslov, S., and Van Der Lelie, D. (2015). Transcriptional responses to sucrose mimic the plant-associated life style of the plant growth promoting endophyte *Enterobacter sp.* 638. PLoS One *10*, e0115455.

22. Pinto-Carbó, M., Gademann, K., Eberl, L., and Carlier, A. (2018). Leaf nodule symbiosis: function and transmission of obligate bacterial endophytes. Curr. Opin. Plant Biol. *44*, 23–31.

23. Danneels, B., Blignaut, M., Marti, G., Sieber, S., Vandamme, P., Meyer, M., and Carlier, A. (2023). Cyclitol metabolism is a central feature of *Burkholderia* leaf symbionts. Environ. Microbiol. *25*, 454–472.

24. Carlier, A., Cnockaert, M., Fehr, L., Vandamme, P., and Eberl, L. (2017). Draft genome and description of *Orrella dioscoreae* gen. nov. sp. nov., a new species of Alcaligenaceae isolated from leaf acumens of *Dioscorea sansibarensis*. Syst. Appl. Microbiol. *40*, 11–21.

25. Spiers, A.J., Bohannon, J., Gehrig, S.M., and Rainey, P.B. (2003). Biofilm formation at the air-liquid interface by the *Pseudomonas fluorescens* SBW25 wrinkly spreader requires an acetylated form of cellulose. Mol. Microbiol. *50*, 15–27.

26. Augimeri, R.V., Varley, A.J., and Strap, J.L. (2015). Establishing a role for bacterial cellulose in environmental interactions: lessons learned from diverse biofilm-producing Proteobacteria. Front. Microbiol. *6*, 1282.

27. Rutherford, S.T., and Bassler, B.L. (2012). Bacterial quorum sensing: its role in virulence and possibilities for its control. Cold Spring Harb. Perspect. Med. *2*, a012427.

28. Waters, C.M., and Bassler, B.L. (2005). Quorum sensing: cell-to-cell communication in bacteria. Annu. Rev. Cell Dev. Biol. *21*, 319–346.

29. Krissinel, E., and Henrick, K. (2007). Inference of macromolecular assemblies from crystalline state. J. Mol. Biol. *372*, 774–797.

30. Pettersen, E.F., Goddard, T.D., Huang, C.C., Meng, E.C., Couch, G.S., Croll, T.I., Morris, J.H., and Ferrin, T.E. (2021). UCSF ChimeraX: structure visualization for researchers, educators, and developers. Protein Sci. *30*, 70–82.

31. Mistry, J., Chuguransky, S., Williams, L., Qureshi, M., Salazar, G.A., Sonnhammer, E.L.L., Tosatto, S.C.E., Paladin, L., Raj, S., Richardson, L.J., et al. (2021). Pfam: the protein families database in 2021. Nucleic Acids Res. *49*, D412–D419.

32. Varadi, M., Anyango, S., Deshpande, M., Nair, S., Natassia, C., Yordanova, G., Yuan, D., Stroe, O., Wood, G., Laydon, A., et al. (2022). AlphaFold Protein Structure Database: massively expanding the structural coverage of protein-sequence space with high-accuracy models. Nucleic Acids Res. *50*, D439–D444.

33. Karimova, G., Pidoux, J., Ullmann, A., and Ladant, D. (1998). A bacterial two-hybrid system based on a reconstituted signal transduction pathway. Proc. Natl. Acad. Sci. USA *95*, 5752–5756.

34. Altinoglu, I., Abriat, G., Carreaux, A., Torres-Sánchez, L., Poidevin, M., Krasteva, P.V., and Yamaichi, Y. (2022). Analysis of HubP-dependent cell pole protein targeting in *Vibrio cholerae* uncovers novel motility regulators. PLoS Genet. *18*, e1009991.

35. Gasteiger, E., Gattiker, A., Hoogland, C., Ivanyi, I., Appel, R.D., and Bairoch, A. (2003). ExPASy: the proteomics server for in-depth protein knowledge and analysis. Nucleic Acids Res. *31*, 3784–3788.

36. Altschul, S.F., Madden, T.L., Schäffer, A.A., Zhang, J., Zhang, Z., Miller, W., and Lipman, D.J. (1997). Gapped BLAST and PSI-BLAST: a new generation of protein database search programs. Nucleic Acids Res. *25*, 3389–3402.

37. Mirdita, M., Schütze, K., Moriwaki, Y., Heo, L., Ovchinnikov, S., and Steinegger, M. (2022). ColabFold: making protein folding accessible to all. Nat. Methods *19*, 679–682.

38. Holm, L. (2022). Dali server: structural unification of protein families. Nucleic Acids Res. *50*, W210–W215.

39. Zheng, S.Q., Palovcak, E., Armache, J.P., Verba, K.A., Cheng, Y., and Agard, D.A. (2017). MotionCor2: anisotropic correction of beam-induced motion for improved cryo-electron microscopy. Nat. Methods *14*, 331–332.

40. Zhang, K. (2016). Gctf: real-time CTF determination and correction. J. Struct. Biol. *193*, 1–12.

41. Punjani, A., Rubinstein, J.L., Fleet, D.J., and Brubaker, M.A. (2017). cryoSPARC: algorithms for rapid unsupervised cryo-EM structure determination. Nat. Methods *14*, 290–296.

42. Emsley, P., Lohkamp, B., Scott, W.G., and Cowtan, K. (2010). Features and development of *Coot*. Acta Crystallogr. D Biol. Crystallogr. *66*, 486–501.

43. Adams, P.D., Afonine, P.V., Bunkóczi, G., Chen, V.B., Davis, I.W., Echols, N., Headd, J.J., Hung, L.W., Kapral, G.J., Grosse-Kunstleve, R.W., et al. (2010). PHENIX: a comprehensive Python-based system for macromolecular structure solution. Acta Crystallogr. D Biol. Crystallogr. *66*, 213–221.

44. Kidmose, R.T., Juhl, J., Nissen, P., Boesen, T., Karlsen, J.L., and Pedersen, B.P. (2019). *Namdinator* – automatic molecular dynamics flexible fitting of structural models into cryo-EM and crystallography experimental maps. IUCrJ *6*, 526–531.

45. Sanchez-Garcia, R., Gomez-Blanco, J., Cuervo, A., Carazo, J.M., Sorzano, C.O.S., and Vargas, J. (2021). DeepEMhancer: a deep learning solution for cryo-EM volume post-processing. Commun. Biol. *4*, 874.

46. Sievers, F., Wilm, A., Dineen, D., Gibson, T.J., Karplus, K., Li, W., Lopez, R., McWilliam, H., Remmert, M., Söding, J., et al. (2011). Fast, scalable generation of high-quality protein multiple sequence alignments using Clustal Omega. Mol. Syst. Biol. *7*, 539.

47. Waterhouse, A.M., Procter, J.B., Martin, D.M.A., Clamp, M., and Barton, G.J. (2009). Jalview, version 2—a multiple sequence alignment editor and analysis workbench. Bioinformatics *25*, 1189–1191.

48. Crooks, G.E., Hon, G., Chandonia, J.M., and Brenner, S.E. (2004). WebLogo: a sequence logo generator. Genome Res. *14*, 1188–1190.

49. Kandiah, E., Giraud, T., de Maria Antolinos, A., Dobias, F., Effantin, G., Flot, D., Hons, M., Schoehn, G., Susini, J., Svensson, O., et al. (2019). CM01: a facility for cryo-electron microscopy at the European Synchrotron. Acta Crystallogr. D Struct. Biol. *75*, 528–535.

50. Matsuyama, B.Y., Krasteva, P.V., and Navarro, M.V.A.S. (2017). Isothermal titration calorimetry to determine apparent dissociation constants (K d) and stoichiometry of interaction (n) of C-di-GMP binding proteins. In c-di-GMP Signaling Methods in Molecular Biology, K. Sauer, ed. (Springer), pp. 403–416.

51. Volke, D.C., Wirth, N.T., and Nikel, P.I. (2021). Rapid genome engineering of *Pseudomonas* assisted by fluorescent markers and tractable curing of plasmids. Bio Protoc. *11*, e3917.

STAR★METHODS

KEY RESOURCES TABLE

REAGENT or RESOURCE	SOURCE	IDENTIFIER
Bacterial strains and oligonucleotides		
See Table S1	This study & Lab collections	N/A
Oligonucleotides		
See Table S2	Eurofins Genomics	N/A
Critical commercial reagents		
Phusion DNA Polymerase	New England Biolabs	Cat# M0530L
DpnI	New England Biolabs	Cat# R0176L
BamHI-HF	New England Biolabs	Cat# R3136L
NotI-HF	New England Biolabs	Cat# R3189L
KpnI-HF	New England Biolabs	Cat# R3142L
EcoRI-HF	New England Biolabs	Cat# R3101L
T4 DNA Ligase	New England Biolabs	Cat# M0202L
T4 Polynucleotide Kinase	New England Biolabs	Cat# M0201L
Quick CIP	New England Biolabs	Cat# M0525S
Deoxynucleotide Set, 100 mM	Sigma-Adrich	Cat# DNTP100A-1KT
Ultrapure IPTG (>99%)	Neo Biotech	Cat# NB-45-00030-25G
OmniPur X-GAL	EMD Millipore	Cat# 9660-1G
Ampicillin sodium salt	Sigma-Aldrich	Cat# A9518-25G
Kanamycin sulfate	Sigma-Aldrich	Cat# 60615-25G
Gentamicin sulfate salt	Sigma-Aldrich	Cat# G1264-1G
3-methylbenzoic acid	Sigma-Aldrich	Cat# 8.21902
Congo Red	Sigma-Aldrich	Cat# C6277-25G
Fluorescent Brightener 28 (CF)	Sigma-Aldrich	Cat# F3543-5G
Tryptone	Sigma-Aldrich	Cat# T9410-1KG
Yeast Extract	EMD Millipore	Cat# 70161-500G
Glycerol	Sigma-Aldrich	Cat# G9012-1L
LB broth with agar	Sigma-Aldrich	Cat# L2897-1KG
LB broth	Sigma-Aldrich	Cat# L3522-1KG
Tryptic Soy Broth / Agar	EMD Millipore	Cat# 22092-500G / 22091-500G
Potassium Phosphate Dibasic	Sigma-Aldrich	Cat# P3786-2.5KG
Potassium Phosphate Monobasic	Fisher	Cat# BP362-1
NaCl	Sigma-Aldrich	Cat# S7653-5KG
HEPES	Sigma-Aldrich	Cat# RDD002-1KG
Imidazole	Sigma-Aldrich	Cat# 792527-1KG
PBS	Sigma-Aldrich	Cat# P4417-100TAB
cOmplete mini, EDTA-free	Roche	Cat# 11836170001
Talon Superflow	Cytiva	Cat# 28957502
PD-10 Columns	Cytiva	Cat# 17085101
Amicon Centrifugal filters	EMD Millipore	Cat# UFC801096 / UFC501024
Superdex 200 Increase 10/300	Cytiva	Cat# 28990944
Mini-PROTEAN TGX 4-20% gels	Bio-Rad	Cat# 4561096
InstantBlue Coomassie stain	abcam	Cat# ab119211
Agarose	Sigma-Aldrich	Cat# A9539-500G
GelGreen Nucleic Acid Stain	EMD Millipore	Cat# SCT124

(*Continued on next page*)

Continued		
REAGENT or RESOURCE	SOURCE	IDENTIFIER
Quantifoil R 1.2/1.3 Au 200 mesh	Quantifoil	Cat# N1-C14nAu20-01
Goat HRP-conjugated anti-His6 antibody	abcam	Cat# ab1269 | RRID: AB_299333
anti-GAPDH antibody	Thermo Fisher Scientific	Cat# MA5-15738 | RRID: AB_10977387
Rabbit HRP-conjugated anti-mouse antibody	abcam	Cat# ab6728 | RRID: AB_955440
ClarityTM Western ECL substrate	Bio-Rad	Cat# 170-5060
Deposited data		
Cryo-EM structure of BcsD$^{O.\ dioscoreae}$	This study	PDB: 8PKD | EMDB: EMD-17735
Cryo-EM structure of BcsD$^{D.\ dadantii}$	This study	PDB: 8POC | EMDB: EMD-17788
Cryo-EM structure of BcsD$^{Enterobacter\ sp.\ 638}$	This study	PDB: 8POG | EMDB: EMD-17791
Software and algorithms		
iTOL	Letunic and Bork[15]	https://itol.embl.de
IDT OligoAnalyzer™ Tool	N/A	https://eu.idtdna.com/calc/analyzer
ExPASy Translate	Gasteiger et al.[35]	https://web.expasy.org/translate/
ExPASy ProtParam	Gasteiger et al.[35]	https://web.expasy.org/protparam/
NCBI BlastP	Altschul et al.[36]	https://blast.ncbi.nlm.nih.gov/Blast.cgi?PAGE=Proteins
PFAM database	Mistry et al.[31]	http://pfam-legacy.xfam.org
WebFlaGs	Saha et al.[18]	https://server.atkinson-lab.com/webflags
AlphaFold2 Protein Structure Database	Varadi et al.[32]	https://alphafold.ebi.ac.uk
ColabFold	Mirdita et al.[37]	https://github.com/sokrypton/ColabFold https://colabfold.mmseqs.com
Dali Structure Comparison Server	Holm[38]	http://ekhidna2.biocenter.helsinki.fi/dali/
PDBePISA	Krissinel and Henrick[29]	https://www.ebi.ac.uk/pdbe/pisa/
ChimeraX	Pettersen et al.[30]	https://www.cgl.ucsf.edu/chimerax/
MotionCor2	Zheng et al.[39]	https://msg.ucsf.edu/software
Gctf	Zhang[40]	https://www2.mrc-lmb.cam.ac.uk/download/gctf/
cryoSPARC	Punjani et al.[41]	https://cryosparc.com/download
Coot	Emsley et al.[42]	https://www2.mrc-lmb.cam.ac.uk/personal/pemsley/coot/
Phenix	Adams et al.[43]	https://phenix-online.org/download/
Namdinator	Kidmose et al.[44]	https://namdinator.au.dk/namdinator/
DeepEMhancer	Sanchez-Garcia et al.[45]	https://github.com/rsanchezgarc/deepEMhancer
Clustal Ω	Sievers et al.[46]	https://www.ebi.ac.uk/Tools/msa/clustalo/
Jalview	Waterhouse et al.[47]	https://www.jalview.org
WebLogo	Crooks et al.[48]	https://weblogo.berkeley.edu/logo.cgi
GraphPad Prism	GraphPad by Dotmatics	https://www.graphpad.com/features

RESOURCE AVAILABILITY

Lead contact

Further information and requests for resources and reagents should be directed to and will be fulfilled by the lead contact, Petya V. Krasteva (pv.krasteva@iecb.u-bordeaux.fr).

Materials availability

Expression constructs and genetically modified bacterial strains generated in this study (Tables S1 and S2) should be requested from and will be provided by the lead contact.

Data and code availability

- All data needed to evaluate the conclusions in the paper are present in the paper and/or the supplemental information. Refined structural models and electron density maps have been deposited in the electron microscopy (emd-17735, emd-17791 and

emd-17788) and protein databanks (pdb-8PKD, pdb-8POG and pdb-8POC) and are publicly available as of the date of publication. Accession numbers are also listed in the key resources table.

- This paper does not report original code.
- Any additional information required to reanalyze the data reported in this paper is available from the lead contact upon request.

EXPERIMENTAL MODEL AND STUDY PARTICIPANT DETAILS

Bacterial strains

Plasmids for heterologous protein expression and bacterial two-hybrid functional complementation assays (see below) were propagated in and isolated from *E. coli* DH5α cells using Lennox LB and LB-agar media supplemented, as applicable, with the following concentrations of antibiotics: 100 μg/ml ampicillin for pProEx-Htb, pUT18 and pUT18C variants and 40 μg/ml kanamycin for pRSFDuet1*, pET-^{His}SUMO and pKT25 variants. All recombinant protein expression for structural and *in vitro* biochemical studies was carried out in *E. coli* BL21 Star™ (DE3) cells using liquid TB (Terrific Broth) media, supplemented with the appropriate antibiotics (see below). Engineering of *O. dioscoreae* mutant strains is described in detail below. *O. dioscoreae* strains were propagated in TSB (Tryptic Soy Broth) liquid medium or on TSA (Tryptic Soy Agar) plates supplemented with 30 μg/ml nalidixic acid due to spontaneous resistance of the model strain *O. dioscoreae* R-71412. No antibiotic was added in the congo red (CR) and calcofluor (CF) binding or biofilm strength assays.

METHOD DETAILS

Recombinant DNA techniques

Recombinant DNA manipulations were carried out using standard protocols for polymerase chain reaction (PCR), molecular cloning, transformation and DNA analysis. Coding regions for BcsH^{CTD} (BcsH$^{292-353}$) of *G. hansenii*; BcsD, BcsP^{FL}, BcsP^{NTD} (BcsP$^{1-80}$), BcsP^{CTD} (BcsP$^{174-230}$), BcsQ and BcsA^{PilZ} (BcsA$^{576-693}$) of *O. dioscoreae*; and BcsD and BcsO of *D. dadantii* were amplified using high-fidelity Phusion DNA polymerase (New England Biolabs) and *G. hansenii*, *O. dioscoreae* and *D. dadantii* genomic DNA as a template. DNA coding for *Enterobacter* sp. 638 proteins BcsD and BcsO were ordered as synthetic, codon-optimized for *E. coli* genes from Invitrogen (GeneArt, Thermo Fisher Scientific) and PCR amplified as above. The PCR products were then introduced by digestion/ligation cloning into isopropyl-β-D-thiogalactopyranoside (IPTG)-inducible expression vectors with custom-modified multiple cloning sites (MCS), as necessary. MCS modifications were performed using inverse PCR-based protocols and mutation-specific oligonucleotides as primers, and PCR products were treated with DpnI restrictase for template DNA digestion prior to ligation and transformation. All restriction enzymes, T4 polynucleotide kinase (PNK), T4 DNA ligase and calf intestinal phosphatase (Quick CIP) used in cloning were purchased from New England Biolabs. Propagated and purified recombinant vectors and introduced mutations were verified by test-digestions and DNA-sequencing.

Protein expression, purification and cryogrid preparation

The coding regions corresponding to *G. hansenii* BcsH^{CTD} (reported previously)[14] and to BcsP$^{O.dioscoreae}$ were PCR amplified and cloned into a modified pProEx-Htb expression vector to yield IPTG-inducible constructs carrying N-terminal hexahistidine (His_6) tags cleavable by the human rhinovirus 3c (HRV3c) protease. In parallel, a standard pRSF-Duet1 vector was PCR-amplified with primers CAT ATG GGA TCC CAT GGT ATA TCT CCT TAT TAA AG and CTC GAG GCG GCC GC A TAA TGC TTA AGT CGA ACA GA to remove the hexahistidine tag-coding region at MCS1 and yield custom-modified pRSFDuet1*, as reported previously.[8,9] The latter was used in BamHI/NotI restrictase-mediated cloning to insert the DNA sequence corresponding to full-length untagged BcsD$^{O.dioscoreae}$ or BcsQ$^{O.dioscoreae}$ for co-expression with pProEX-Htb-encoded BcsH$^{CTD\text{-}G.hansenii}$ or BcsP$^{O.dioscoreae}$, respectively. Coding regions for BcsD from *D. dadantii* and *Enterobacter* sp. 638 were cloned by restriction/ligation based cloning into a modified pET-^{His}SUMO plasmid, yielding a hexahistidine-tagged Ulp1-cleavable SUMO moiety fused to the N-terminus of the protein of interest.

For recombinant protein expression, all expression vectors were freshly (co-)transformed into chemically competent *E. coli* BL21 Star™ (DE3) cells and plated onto antibiotics-supplemented LB-agar plates (100 μg/ml ampicillin, 40 μg/ml kanamycin or a combination of 70 μg/ml ampicillin + 30 μg/ml kanamycin for co-expressed vectors). Resultant colonies were then inoculated and grown aerobically at 37°C in terrific broth (TB) medium supplemented with the appropriate antibiotics as above. At a cell optical density corresponding to light absorbance of 0.8-1.2 at 600 nm wavelength (OD_{600}), the cells were moved to 17°C and overnight protein expression was induced by the addition of IPTG at a final concentration of 0.7 mM. After 16 hours, the cells were harvested by centrifugation (20 minutes at 4000 g and 4°C) and resuspended in the appropriate lysis buffer.

BcsD of *O. dioscoreae* was purified as an untagged pRSFDuet1*-cloned construct via co-expression with and co-purification through Bcs^{His}H^{CTD} of *G. hansenii* (cloned in pProEx-Htb).[14] Following overnight protein expression and culture pelleting, the cells were resuspended in lysis buffer containing 20 mM HEPES pH 8.0, 100 mM NaCl, 17 mM Imidazole pH 8.0 and 1 tablet/50 ml cOmplete mini EDTA-free protease inhibitors (Roche) and flash-frozen in liquid nitrogen. For protein purification, cells were thawed and lysed by sonication. Cell debris were removed by centrifugation (1 h at 48 000 g and 4°C) and the cleared lysates were loaded onto buffer-washed Talon Superflow™ resin (GE Healthcare) at approximately 0.5 ml of resin per liter of culture. The resin was

subsequently washed with more than 30 volumes of IMAC buffer A (protease inhibitor-free lysis buffer as above) and bound proteins were eluted in a single step with IMAC buffer B (IMAC buffer A supplemented with 200 mM Imidazole pH 8.0). The eluted protein was concentrated and subjected to gel filtration through a Superdex 200 Increase 10/300 GL column using buffer containing 20 mM HEPES pH 8.0 and 250 mM NaCl. Peak fractions were analyzed by SDS-PAGE and Coomassie staining and fractions corresponding to BcsD were collected, concentrated and buffer-exchanged on the same gel filtration column in buffer containing 20 mM HEPES pH 8.0 and 100 mM NaCl. Eluted protein fractions were pooled, concentrated and used for cryogrid preparation. Briefly, gold Quantifoil R 1.2/1.3 grids were glow discharged in air (ELMO system, Cordouan Technologies) and the protein sample was applied and cryo-plunged in liquid ethane using a Vitrobot Mark IV system (Thermo Fisher Scientific) operated at 100% chamber humidity and 4°C. Excess protein aliquots were flash-frozen in liquid nitrogen for subsequent use in isothermal titration calorimetry (ITC) experiments.

BcsP of *O. dioscoreae* was cloned as an N-terminally hexahistidine-tagged constructs in pProEx-Htb, however no significant protein expression was observed under growth, induction and purification as above. Nevertheless, upon co-expression with pRSFDuet1*-cloned $BcsQ^{O.dioscoreae}$, the same construct showed markedly improved recombinant expression and was IMAC-purified as BcsD above. The IMAC-eluted protein was mixed with His_6-tagged recombinantly expressed HRV3c for removal of the N-terminal affinity tag, concentrated to 2.5 mL and buffer exchanged in buffer containing 20 mM HEPES pH 8.0, 100 mM NaCl and 12 mM Imidazole using a disposable PD-10 desalting column. The elution fraction was then incubated overnight and the epitope-free protein was collected in the flow-through fraction during reverse IMAC purification on the following day. Following concentration the protein was subjected to two-step gel filtration as BcsD above.

For purification of BcsP-bound BcsD, the latter was incubated with excess BcsP and subjected to gel filtration (buffer: 20 mM HEPES pH 8.0 and 100 mM NaCl). Eluted protein-containing fractions corresponding to an earlier absorbance peak relative to the input BcsP and BcsD proteins were concentrated and used for cryogrid preparation as above.

Coding sequences for BcsD of *D. dadantii* and *Enterobacter* sp. 638 were cloned into a modified pET-^{His}SUMO vector, yielding a hexahistidine-tagged Ulp1-cleavable SUMO moiety fused to the N-terminus of the protein of interest. Cells were grown, induced, pelleted and lysed as above. Clarified lysates were subjected to IMAC as above and the eluted proteins were mixed with His_6-tagged recombinantly expressed Ulp1 protease for removal of the N-terminal ^{His}SUMO moiety. Following concentration, buffer exchange, overnight incubation and reverse IMAC as above, the epitope-free proteins were concentrated, subjected to gel filtration (20 mM HEPES pH 8.0 and 100 mM NaCl) and used for cryogrid preparation.

Gel filtration and SDS-PAGE analyses of the purified protein samples are shown in Figures S5A–S5D.

SDS-PAGE and Western Blot analysis

Protein fractions were analyzed by standard denaturing SDS-PAGE electrophoresis using 4-20% gradient mini-gels (Bio-Rad), Abcam InstantBlue™ Coomassie stain and a Gel Doc™ EZ system (Bio-Rad) for Coomassie stain visualization. For western blot analyses SDS-PAGE migrated proteins were directly transferred using a standard mini-gel transfer protocol, PVDF membranes and a Trans-blot® Turbo transfer system (Bio-Rad). Blocking and antibody incubations were done in the presence of 5% skim milk in TPBS (Phosphate Buffered Saline with 0.1% Tween-20), all washes between and after antibody incubations were done with 1x TPBS buffer. Goat HRP-conjugated anti-His_6 (abcam, ab1269, dilution 1:1000) antibody was used for hexahistidine tagged protein detection and a combination of an anti-GAPDH (Thermo Fisher Scientific, #MA5-15738; dilution 1:1000) primary and a rabbit HRP-conjugated anti-mouse secondary (abcam, ab6728, dilution 1:10000) antibodies were used for GAPDH detection as a loading control. Signals were visualized using the Clarity™ Western ECL substrate and a ChemiDoc™ imaging system (Bio-Rad).

Cryo-EM and single-particle analysis (Cryo-SPA)

A preliminary dataset on *O. dioscoreae* BcsD was collected at 200 kV on the Elsa Talos Arctica transmission electron microscope (Thermo Fisher Scientific) at the European Institute of Chemistry and Biology (IECB Bordeaux, France), equipped with a Gatan K2 Summit direct electron detector (DED) and operated with SerialEM in counting mode. A total of 4,077 movies were collected with a total electron dose of ~50 $e^-/Å^2$ and a corrected pixel size of 0.93 $Å^2$. The movies were motion- and CTF-corrected using MotionCor2[39] and Gctf,[40] respectively, after which 3,709 micrographs with defocus range 0.6-2.5 μm and resolutions better than 5 Å were kept for further processing in cryoSPARC v3 and v4.[41] Particles were autopicked using the software's 'Blob picker' function and after 2D classification, the best-resolved representative views (2D class averages) were used as templates for new rounds of template-based autopicking, 2D classifications and data clean-up. A total of 41,385 particles corresponding to 2D class averages with well-aligned features were used for *Ab-initio* model generation and non-uniform (NU-) refinement. The resultant 3D electron density map featured ~5.5 Å resolution sufficient to determine the oligomeric state and intrinsic symmetry of *O. dioscoreae* BcsD.

To increase the resolution and reliably interpret the 3D electron density map we resorted to data collection on optimized cryogrids using the 300 kV CM01 Titan Krios microscope (ESRF, Grenoble, FR)[49] equipped with a K3 direct electron detector and a Gatan GIF Quantum LS energy filter. A total of 19,118 movies (51.6 $e^-/Å^2$ and 0.657 Å pixel size) were motion- and CTF-corrected as above and 17,033 micrographs with resolution higher than 4.5 Å and defocus range of 0.4-2.5 μm were retained for further analysis in cryoSPARC. A total of 6,563,631 particles were picked using the software's 'Template picker' function, extracted in a 300-pixel box and subjected to 2D classification. Well-resolved class averages containing a total of 2,478,376 particles were retained and input for *ab-initio* model generation with three 3D classes, followed by heterogeneous refinement. Two of the resultant 3D models differed essentially by the handedness of the reconstructed density maps and their corresponding particles were used together as input in NU-refinement with D2 symmetry to obtain the final 3D map at 2.3 Å resolution. To facilitate model building and refinement the map

was sharpened using the DeepEMhancer tool[45] through the cryoSPARC interface. The atomic model was refined against the experimental and sharpened maps using the AlphaFold2[32] prediction as a starting model, manual building and regularization in Coot[42] and automated real-space refinement in Phenix.[43]

Cryogrids with *D. dadantii* BcsD were imaged at the Elsa Talos Arctica microscope as above. 3,379 movies were collected with a total electron dose of ~47 $e^-/Å^2$ and a corrected pixel size of 0.93 $Å^2$. The movies were motion- and CTF-corrected as above, after which 3,168 micrographs with defocus range 0.6-2.5 μm and resolutions better than 5 Å were kept for further processing in cryoSPARC. Particle picking was done via the software's 'Blob picker', 2D classification, 2D select and 'Template picker' functions. A total of 1,488,279 picked particles were then 2D classified and of these 406,652 particles corresponding to well-resolved 2D class averages were used for *Ab-initio* model generation and Hetero Refinement with 2 classes. The dominant class corresponding to 295,199 particles was then input for NU-refinement with D2 symmetry and the resultant map (resolution 3.94 Å) was sharpened using DeepEMhancer.[45] The atomic model was built using a ColabFold[37] prediction for the tetrameric *D. dadantii* BcsD as a start model and refinement against the sharpened cryo-EM map using Coot, Phenix and Namdinator.[42–44]

Cryogrids with *Enterobacter* sp. 638 BcsD were imaged at the Elsa Talos Arctica microscope as above. 5,949 movies were collected with a total electron dose of ~49 $e^-/Å^2$ and a corrected pixel size of 0.93 $Å^2$. The movies were motion- and CTF-corrected as above, after which 5,226 micrographs with defocus range 0.4-2.6 μm and resolutions better than 5.5 Å were kept for further processing in cryoSPARC. Particle picking was done via the software's 'Blob picker', particle extraction, 2D classification, 2D select and 'Template picker' functions. Following particle re-extraction and two rounds of 2D classification, a total of 408,125 particles from well-resolved class averages were used for *Ab-initio* model generation and Hetero Refinement with 2 classes. The dominant class corresponding to 226,283 particles was then input for NU-refinement with D2 symmetry and the resultant map (resolution 4.15 Å) was sharpened using DeepEMhancer.[45] The atomic model was built using a ColabFold prediction for the tetrameric *Enterobacter* sp. 638 BcsD as a start model and refinement against the sharpened cryo-EM map using Coot, Phenix and Namdinator.[42–44]

Data collection and coordinate refinement statistics are summarized in Table S3 and the EM data processing strategies are shown in Figures S5E–S5G.

Isothermal Titration Calorimetry (ITC)

The direct BcsD-BcsP interactions were corroborated and further characterized by ITC using a Microcal VP-ITC calorimeter from Malvern Panalytical at 20°C. Purified BcsD was concentrated to 160 μM and was titrated into 10 μM purified BcsP or the protein-free gel filtration buffer (20 mM HEPES pH 8.0 and 100 mM Imidazole pH 8.0). Protein concentrations were determined by a combination of methods including a colorimetric assay (RC DCTM, Bio-Rad) and 280 nm absorbance measurements (A280), while accounting for potential scattering contributions (A330).[50] ITC data were analyzed by integrating the injection heat effects, normalized to the amounts of proteins present in the sample cell and injection syringe, and curve-fitting using a single-site binding model within the Origin software package for Microcal. The BcsD into buffer titration was performed to account for heat dilution effects and the latter were subtracted during the BcsP binding analysis. The apparent dissociation constant (Kd) and stoichiometry of interaction (N) were derived from the data using standard procedures and the graphs were replotted using the GraphPad Prism software.

Bacterial two-hybrid assay (BACTH)

To probe protein-protein interactions *in cellulo*, we resorted to the bacterial split adenylate cyclase two-hybrid complementation assay (BACTH).[33] By PCR amplification we first custom-modified the standard expression vectors pKT25, pUT18 and pUT18C as described previously,[8,9,14] in order to introduce BamHI and KpnI cloning sites in the respective multiple cloning sites (MCS), while optimizing the number and type of exogenous amino-acids to be added to the recombinant hybrids (Data S1). Coding regions for full-length BcsD from *O. dioscoreae*, *D. dadantii* and *Enterobacter* sp. 638; $BcsA^{PilZ}$, BcsQ, and BcsP variants from *O. dioscoreae*; and BcsO from *D. dadantii* and *Enterobacter* sp. 638 were then PCR amplified with primers carrying the corresponding restriction sites, digested and ligated into the modified vectors. All recombinant constructs were amplified in DH5α cells and verified by DNA sequencing. The bacterial two-hybrid assay was performed using standard protocols and the *E. coli* bEYY2122 strain (BTH101 *Δcya*).[34] Briefly, chemically competent *E. coli* bEYY2122 cells were co-transformed with derivatives of the pUT18(C) and pKT25 vectors and plated on LB Miller-agar supplemented with 70 μg/ml ampicillin and 30 μg/ml kanamycin. Individual co-transformant colonies were picked and grown overnight at 37°C in liquid antibiotics-supplemented LB medium. The next morning, 4 μl of saturated culture were spotted onto LB Miller-agar plates supplemented with 70 μg/ml ampicillin, 30 μg/ml kanamycin, 0.1 mM IPTG, and 40 μg/ml X-gal. Protein interactions were evaluated after 24 h incubation at 30°C by blue colony color. pUT18C and pKT25 vectors carrying the corresponding adenylate cyclase fragments but no recombinant fusions were used in co-transformations as negative controls, whereas co-transformants expressing pKT25-zip and pUT18C-zip vectors were used as positive controls. The latter vectors are derivatives of the pKT25 and pUT18C vectors in which the leucine zipper of Gcn4 (amino acid sequence: … I Q R M K Q L E D K V E E L L S K N Y H L E N E V A R L K K L V G E R) is genetically fused in frame to the T25 and T18 adenylate fragments, respectively.[33] The results are representative of at least 3 independent experiments and more than 6 biological replicates.

O. dioscoreae gene deletions

To generate Δ*bcsD*, Δ*bcsA*, Δ*bcsP* and Δ*wssH* in-frame deletion mutants in *O. dioscoreae* while preserving downstream start codons and 5' Shine-Dalgarno sequences, we adapted a protocol originally designed for genetic engineering of *Pseudomonas putida* based on the use of a suicide vector, pSNW2.[51] Briefly ~500-bp DNA fragments upstream and downstream of *bcsD, bcsA*, and *wssH*

were PCR amplified using *O. dioscoreae* genomic DNA as a template. The fragments were then fused using overlap-extension PCR, cloned into the pCR-BluntII-TOPO vector (Invitrogen) to yield pTOPO-Δ*bcsD*, pTOPO-Δ*bcsA* and pTOPO-Δ*wssH*, sequence-verified and subcloned using EcoRI restriction-based cloning into the pSNW2 suicide vector to yield pSNW2-Δ*bcsD*, pSNW2-Δ*bcsA* and pSNW2-Δ*wssH*, respectively. Upstream and downstream sequences of DNA for Δ*bcsP* were ordered as a plasmid-borne synthetic construct from Invitrogen (GeneArt, Thermo Fisher Scientific) and sub-cloned into pSNW2 using EcoRI to yield pSNW2-Δ*bcsP*. The suicide vectors were maintained in the *E. coli* strain CC118λpir and mobilized into *O. dioscoreae* with the help of the *E. coli* 1047 strain carrying the conjugative plasmid pRK2013. As the first recombination event results in the integration of the pSNW2 derivative carrying the entire "mutator" vector inserted into the chromosome, successful recombinants were selected on TSA supplemented with 30 μg/ml nalidixic acid and 40 μg/ml kanamycin, and were green-fluorescent due to mGFP encoded in pSNW2.

The second recombination event was then performed by mobilizing pQURE6-H in the above recombinants in the presence of 1 mM 3-methylbenzoate (3-mBz, for plasmid replication) and 10 μg/ml gentamicin (resistance gene on pQURE6-H, for plasmid maintenance). As the pQURE6-H vector encodes the SceI homing endonuclease,[51] target sites for which are found on the inserted pSNW2 plasmid but not elsewhere on the *O. dioscoreae* genome, double recombinants with ejected pSNW2 backbone were selected on TSA supplemented with 30 μg/ml nalidixic acid, 10 μg/ml gentamicin and 1 mM 3-mBz, and were red-fluorescent due to mRFP encoded in pQURE6-H. Clones were then propagated in TSB in absence of 3-mBz to cure the pQURE6-H plasmid and were then verified by PCR amplification and DNA sequencing.

Phenotypic assays of cellulose secretion and biofilm strength

Wild-type and mutant *O. dioscoreae* colony morphotypes were evaluated on antibiotics-free TSA with or without 0.002% calcofluor (CF or Fluorescent Brightener 28, Sigma-Adrich) or 25 μg/mL congo-red (CR, Sigma-Adrich). Single colonies were inoculated in 2 mL of nalidixic acid-supplemented TSB and grown to stationary phase under agitation (24 h at 30°C). 4 μL of each culture were spotted onto TSA plates and incubated in the dark at 30°C for 4 days. Images were taken under transmission white light for TSA-only and TSA-CR plates and under 365 nm UV light illumination for the TSA-CF plates. For visual inspection of cellulose secretion at the air-liquid interface (ALI), 5 μL of stationary phase *O. dioscoreae* liquid cultures grown as above were inoculated in 5 mL of CF-supplemented TSB and grown under static conditions for 4 days at 30°C. Images were taken under 365 nm UV light illumination.

For evaluation of attachment strength of the cellulosic biofilm pellicles formed at the ALI, 5 μL of stationary phase *O. dioscoreae* liquid cultures were inoculated in 5 mL of supplement-free TSB and grown at 30°C under static and dark conditions for 4 days. ALI biofilm strength was measured as the average mass of glass microbeads (0.45-0.5 mm, Sartorius) needed to break through each pellicle[25] and normalized relative to wild-type *O. dioscoreae* with 12 independent replicates for each strain.

Additional bioinformatics tools

Primer design was optimized using the IDT OligoAnalyzer™ tool. DNA and/or protein sequences and structures were analyzed using the ExPASy Translate and ProtParam tools,[35] the NCBI BlastP suite,[36] the PFAM database,[31] WebFlaGs,[18] the AlphaFold2 structure prediction database[32] and ColabFold,[37] the DALI structure comparison server,[38] and the PDBePISA macromolecular interface and structure exploration server.[29] Structure visualization was done in ChimeraX.[30] Multiple sequence alignments and phylogenetic tree visualization were done in Clustal Omega,[46] Jalview[47] and iTOL,[15] respectively.

QUANTIFICATION AND STATISTICAL ANALYSIS

The experiments in this study were not randomized and the researchers were not blinded during experimental design, execution or outcome assessment. Nevertheless, many of the experiments were reproduced independently by different investigators, including electron microscopy, biochemical and phenotypic assays.

Figure 2B represents biofilm strength measurements (see method details), mean and SEM for 12 independent replicates for each of the *O. dioscoreae* genetic backgrounds. Data normalized to wild-type.